Meridional Heat Transport during Atmospheric Rivers in High Resolution CESM Climate Projections

Christine A. Shields[1], Nan Rosenbloom[1], Susan Bates[1], Cecile Hannay[1], Aixue Hu[1], Ashley E. Payne[2], Jonathan J. Rutz[3], John Truesdale[1]

[1]National Center for Atmospheric Research, Boulder, Colorado, 80302

[2]University of Michigan, Ann Arbor, MI 48109

[3]National Oceanic and Atmospheric Administration, Salt Lake City, UT 84138

Corresponding author: Christine A. Shields (shields@ucar.edu)

Key Points:

- Heat transport during landfalling atmospheric rivers is explicitly computed for Western North America and Europe.
- Under global warming, latent heat transport increases across all regions in the mid-latitudes where sensible heat decreases (increases) for Western North America (Europe).
- Upper-level meridional wind component dominates changes in heat transport.

This is the author manuscript accepted for publication and has undergone full peer review but has not been through the copyediting, typesetting, pagination and proofreading process, which may lead to differences between this version and the Version of Record. Please cite this article as doi: 10.1029/2019GL085565

Abstract

Meridional sensible and latent heat transport is evaluated for regions with landfalling atmospheric rivers using both MERRA-2 reanalysis and fully coupled CESM1.3 high-resolution climate projections. Western North America, the United Kingdom, and the Iberian Peninsula are chosen to represent regions significantly impacted by atmospheric rivers (ARs). CESM1.3 historical simulations can accurately represent both sensible and latent regional meridional heat transports compared to MERRA-2 both for the total period analyzed (1980 – 2016) and for days with atmospheric rivers only. Uncertainty in these calculations due to AR identification is assessed by applying available Tier 1 AR-catalogues from Atmospheric Tracking Method Intercomparison Project (ARTMIP) to the MERRA-2 analysis. CESM1.3 climate projections suggest that under global warming, latent heat transport increases across all regions in the mid-latitudes where sensible heat decreases (increases) for Western North America (Europe). Generally, changes to the meridional heat transport are forced by the upper-level meridional wind component.

Plain Language Summary

Atmospheric rivers (ARs) are long, filamentary structures in the atmosphere that transport significant amounts of water and energy from lower latitudes to higher latitudes. They can be considered a subset of an extratropical storm and are commonly found in the mid-latitudes. To

date, the majority of research has focused on water transport simply because ARs are an important part of Earth's hydrological cycle and can act as either drought-busters or mechanisms for catastrophic floods, particularly in regions such as western North America and western Europe. Here, rather than focusing on water transport, we analyze two key contributors to total energy transport in the atmosphere: (1) heat produced by the phase changes of water (latent heat), and (2) heat produced by a change in temperature (sensible heat). With global warming, for days with landfalling atmospheric rivers, we find that sensible heat transport decreases for western North America but increases for western Europe. Latent heat transport, however, increases across all regions.

1 Introduction

Atmospheric rivers (ARs) are typically known for their ability to transport large amounts of moisture from tropical and sub-tropical locations into the mid and high latitudes (Bonne et al., 2015; Dettinger, 2011; Dettinger et al., 2011; Gorodetskaya et al. 2014; Ralph et al., 2004, 2005, 2011, 2013). They provide relief to drought-stricken communities (Dettinger, 2013), or they can inundate coastal locations, causing floods and natural disasters, such as the Oroville Dam Crisis in northern California in the winter of 2017 (Vahedifard et al., 2017). Much of the research to date has focused on the hydrological cycle aspects of ARs with examples from identifying moisture sources and impacts of aerosols (Dacre et al., 2015, Ramos et al. 2016, Ralph et al., 2017a) to evaluating extreme precipitation and its impacts on the water table, snowpack, and local communities (Neiman et al., 2008; Neiman et al., 2011; Guan et al., 2012; Lavers et al., 2012; Lavers and Villarini, 2013; Lavers and Villarini, 2015). Research has also been conducted on widely different climate regimes from paleoclimate, (e.g., Last Glacial Maximum, Lora et al. 2017, and Eocene, Kiehl et al., 2018), to future climates under global warming (Chang et al., 2012; Espinoza et al. 2018; Hagos et al., 2016; Lavers et al., 2013; Lavers et al., 2015; Mizuta,

2012; Payne and Magnusdottir, 2015; Shields and Kiehl, 2016a, b; Warner et al., 2015). However, other than quantifying the thermodynamical contributions of moisture transport under climate change (Gao et al., 2015, 2016; Sousa et al. 2019), and investigating air temperature within the ARs themselves, (Gonzales et al., 2019), little research has been devoted to investigating the energy transport explicitly by atmospheric rivers. Understanding energy changes within ARs is an important new direction identified by the scientific community (Ralph et al. 2017b).

In the total energy budget, meridional features are the primary mechanism that carries energy poleward (Barry et al., 2002). There have been numerous studies looking at the changes in the storm track under global warming (e.g., O'Gorman, 2010; Tamarin-Brodsky and Kaspi, 2017) as well as theoretical and modeling studies from the lens of energy transport (Colman et al. 1994; Wu et al., 2010; Siler et al. 2018; Armour et al., 2019). For our study, we specifically focus on atmospheric rivers, (a subset of mid-latitude storms), and evaluate meridional heat transport over three regions commonly impacted by landfalling ARs, (1) western North American, (2) the United Kingdom, and (3) the Iberian Peninsula. As a first step toward understanding the contribution of ARs to the meridional heat transport, we focus on the sensible and latent heat transports (SHT, LHT respectively). This work is organized as follows: In section 2, we present details and methodology for both MERRA-2 and CESM1.3 datasets. Catalogues from Tier 1 ARTMIP (Atmospheric River Tracking Method Intercomparison Project) are applied to address

uncertainty due to AR detection methodology (Shields et al. 2018a, b; Rutz et al., in revision). In section 3, we evaluate heat transport by atmospheric rivers using a) the MERRA-2/ARTMIP analysis, b) the CESM1.3 historical simulations compared to the MERRA-2, and c) the CESM1.3 climate change simulations. Section 4 discusses the primary mechanism behind the meridional heat transport climate response and section 5 summarizes our work.

2 **Data and Methods**

2.1 MERRA-2 Reanalysis and ARTMIP

MERRA-2 (Modern Era Retrospective-Analysis for Research and Applications, (Gelaro et al., 2017, Data DOI number: 10.5067/QBZ6MG944HW0) reanalysis data, is used for this work to approximate observations. The period, 1980-2016, was chosen to encompass ARTMIP data so a systematic comparison between methodologies could be accomplished as well as quantifying uncertainties in the heat transport quantities simply due to the detection algorithm. ARTMIP is a grassroots effort designed to provide the community with a means of quantifying uncertainties in AR science due to the many detection algorithms currently used and found in the literature (Shields et al. 2018, also see ARTMIP website: http://www.cgd.ucar.edu/projects/artmip/). Drawing on catalogues available through ARTMIP, heat transport is computed for ARTMIP MERRA-2 catalogues to determine the spread amongst the methodologies (Supplemental Table

1; Brands et al., 2016; Gershunov et al., 2017; Goldenson et al., 2018; Guna and Waliser, 2015; Hagos et al., 2016; Lavers et al., 2012; Lora et al., 2017; Mundhenk et al., 2016; Muszynski et al., 2018; Payne and Magnusdottir, 2014, 2015; Ramos et al., 2016; Rutz et al., 2014; Sellars et al., 2015, Shields and Kiehl 2016a,b). Heat transport equations (1) and (2) are shown in Section 3 and employ full 3d-field daily reanalysis fields for wind, temperature, and specific humidity. AR tracking is done at 3-hourly intervals, as per ARTMIP design.

2.2 CESM1.3 Model Description and Simulations

CESM1.3 is the high-resolution version of the standard Community Earth System Model (version 1.3), but with several modifications documented in Meehl et al. (2019). The atmosphere component is CAM5 (Neale et al. 2010; Park et al. 2014) and employs the spectral element dynamical core (Taylor and Fournier, 2010; Dennis et al. 2012) at 0.25^{o} resolution(ne120) unlike other standard 1^{o} CESM1 simulations (Hurrell et al. 2013). The land component is CLM4 (Lawrence et al. 2011) at 0.25^{o} resolution, and the river transport model is RTM, at 0.5^{o} resolution. The ocean component is POP2 (Smith et al. 2010, Danabasoglu et al. 2011), and the ice component is CICE4 (Hunke and Lipscomb, 2008), where both the ocean and ice are integrated at a nominal 1^{o} resolution. The high-resolution version of CESM is the preferred configuration because increasing horizontal resolution has been shown to better represent the regional hydrological cycle and ARs in particular (Hagos et al. 2015, Shields et al. 2016c).

Ensemble simulations for both historical and RCP8.5 (Representative Concentration Pathway) experiments were analyzed, although due to some data loss, parts of this analysis did not use all members (supplemental Table S2). Years 1960-2005 (historical simulations, three ensemble members) and 2070-2099 (RCP8.5 simulations, two ensemble members) were included for all AR tracking and statistics, at 6-hourly intervals (see supplemental Figures S1 and S2 for AR tracking statistics compared to MERRA-2). Heat transport terms were taken from mean 3-hourly data and averaged to daily frequency to match the MERRA-2 data. High-temporal frequency output is available for heat transport calculations (full field wind, moisture, and temperature) for model years 1991-2005 (historical, one ensemble member) and 2070-2099 (RCP8.5, one ensemble member), although only annual data representing the mean states are presented here. Seasonal cycle climatologies were computed using monthly data, years 1960-2005 and 2070-2099, respectively.

Section 2.3 AR detection for Climate Change

For CESM1.3 data, the Shields and Kiehl algorithm (Shields and Kiehl 2016a; 2016b), henceforth called SK2016, is specifically chosen to detect ARs for CESM1.3 data because it was uniquely developed to detect ARs for high-resolution climate change projections. Three regions are targeted for landfalling ARs: (1) western North America (32°-52°N, henceforth called

WNAM), (2) United Kingdom (49°-60°N, UK), and (3) the Iberian Peninsula (35°-49°N, Ib). ARs are required to be longer than they are wide (requiring a 2:1 grid point ratio and a length of at least 200 km), the 850hPa wind direction must be from the southwest (180 – 270^{o}) for western North America and have a westerly aspect (180-360^{o}) for western European regions. The 85th percentile of the magnitude of the 850hPa wind vector is computed to impose a minimum wind strength threshold. It is computed self-consistently from the dataset where ARs are being detected. The primary control is the moisture anomaly field where total column water (i.e., integrated water vapor, IWV), is computed using an empirical formula provided in Zhu and Newell (1998), tested in Newman et al. (2012), and also used by Gorodetskaya et al. 2014. Moisture thresholds are based on spatial anomalies and are calculated for each latitudinal band using both the zonal mean and maximum values for IWV. The moisture threshold reference value is then used at each grid point along the coastline to determine if AR conditions exist for each 3-hour interval. The SK2016 detection algorithm is designed to extract stronger storms and ignore weak ones, and thus, is one of the most restrictive algorithms in the ARTMIP suite (Rutz et al. in revision). Comparing the SK2016 to the ARTMIP spread allows the reader to understand how this method varies from others regarding meridional heat transport calculations.

3 Heat Transport in Landfalling Atmospheric Rivers

Similar to Colman et al. (1994), we define sensible and latent heat energy transports as follows:

$$\mathrm{SHT} = \int_{\mathrm{Pbot}}^{\mathrm{Ptop}} \frac{1}{\mathrm{g}} (cp\ v\mathrm{T})\ \mathrm{dp} \qquad (1)$$

$$\mathrm{LHT} = \int_{\mathrm{Pbot}}^{\mathrm{Ptop}} \frac{1}{\mathrm{g}} (L\ v\mathrm{q})\ \mathrm{dp} \qquad (2)$$

where SHT signifies sensible heat transport, LHT is latent heat transport, *cp* is the specific heat constant, *L* is the latent heat of vaporization, *g* is gravity, T is temperature, q is specific humidity, and *v* represents the meridional wind. P_{top} and P_{bot} represent the top and bottom pressure layers and the integral limits (for model or reanalysis data, P_{top} is represented by the pressure at the tropopause). Total atmospheric energy transport also includes potential energy; however, we do not consider potential energy here because our focus is climate change and mechanical energies have been shown to have a small or negligible effect (Pan et al., 2017). Only landfalling ARs are evaluated and isolated over the targeted regions so that heat transport data can be explicitly calculated without influence from other AR-like structures and/or significant moisture transports such as monsoonal flows and tropical cyclones.

Heat transport data is computed daily for the full period (i.e., Equations 1 and 2 are solved for each day from 1991-2005). We refer to the daily heat transport for the full period as "All-days." Within this dataset, a subset of days with atmospheric rivers are referred to as "AR-days." These "AR-days" are days where catalogues register AR conditions at any interval during that calendar day. All-days and AR-days are composited into annual means and transport is computed across

the regional boundary. Annual composites of MERRA-2 SHT (left panels, red) and LHT (right panels, green) are shown in Figure 1 for All-days (heavy, black lines), the ARTMIP spread (shaded), and ARTMIP median values (color dashed). MERRA-2 AR-days identified by the SK2016 algorithm are superimposed as a black dashed line. Longitudinal bounds are noted in the above each panel on the right and scaled by the great circle distance to produce the conventional unit of PW. The broad longitudinal swaths shown incorporate not only the coastal regions where ARs make landfall, but also upwind oceanic regions impacted during the AR life cycle.

Each row of Figure 1 shows a different region; WNAM is shown in the upper panels, the UK in the middle panels, and the Ib in the lower panels. Note that although the UK and Ib domains are computed across the same longitudinal bounds, and plotted from 20°N to 60°N, the difference between these panels highlights the difference between synoptic-scale ARs making landfall over the UK, and those making landfall over the Iberian Peninsula. Although they are broadly similar, there are some differences between the European regions, especially for LHT where there is a larger ARTMIP spread and broader transport across the mid-latitudes for the Iberian Peninsula. This spread could, in small part, be due to different number of algorithms that specifically target the Iberian Peninsula, (see supplemental Table S1). The ARTMIP spread illustrates the general agreement in heat transport across different algorithms. The SK2016 algorithm tends to be closer to the maximum value for SHT, and closer to the median in the mid-latitudes (40^{o}-60^{o}N) for LHT. Given the SK2016 is designed to detect stronger storms, it is not surprising that this

algorithm appears closer to the maximum for SHT values. Also worthy of note is that for most cases, AR-days (median and maximum) tend to exceed All-days in the mid-latitude bands where ARs are most active.

Figure 2 shows a comparison of heat transport quantities in CESM1.3, a sophisticated fully coupled earth system model, against the MERRA-2 reanalysis. Both AR-days (dashed lines) and All-days (solid lines) are shown for the same regions as in Figure 1. Relative to MERRA-2, the model estimates both the latitudinal distribution of heat transport and its absolute value (shown as PW) reasonably well. AR-days (dashed) for both MERRA-2 and CESM1.3 clearly transport more sensible heat for WNAM in the mid-latitudes compared to All-days, although this relationship is less pronounced for European ARs, which is also seen in Figure 1. For all regions, LHT AR-days (dashed) exceeds All-days for most latitudes with general agreement between CESM1.3 and MERRA-2. The exception to this relationship is seen for WNAM and the Iberian Peninsula, where in the upper mid-latitudes, LHT All-days (solid) exceed AR-days.

Finally, SHT and LHT are computed for both the historical and RCP8.5 simulations (Figure 3) for the same regions and domains as in Figures 1 and 2. The historical simulation is shown in red for SHT and green for LHT, whereas the RCP8.5 is purple for the respective panels. Dashed lines are AR-days and solid lines are All-days. As one might expect, for WNAM, a region dominated by ARs originating deeper into the tropical and subtropical bands, SHT is reduced for both AR-days and All-days for the mid-latitudes, although ARs are still carrying more heat, on average, than All-days. The European regions are projected by CESM1.3 to receive a modest

increase in heat transport for the mid-latitudes, an area that is dominated by the eddy driven jet and where heat and moisture are sometimes sourced from both lower mid-latitude and subtropical bands. LHT is projected to increase for all the regions northward of 40^{o}N, regardless of AR subsetting. AR-days (dashed), however, are offset equatorward compared to All-days (solid), consistent with ARs dominating moisture transport at these latitudes. Although all areas experience an increase in LHT (purple lines), it is only across WNAM under global warming that AR-days shift poleward by ~2^{o} of latitude, (green dashed versus purple dashed).

Figures 1-3 have focused on the broader AR life cycle regions; however, examining the spatial fingerprint for each region is important when looking at climate change mechanisms as discussed in Section 4. At the coastlines (Supplemental Figures S3 and S4), ARs tend to carry more heat compared to All-days (not shown) but are very similar to Figure 3. The exception is WNAM, where the climate change due to global warming is different for the coastline domain compared to the life cycle region. For the greater domain, SHT is projected to decrease, and along the coastline and over the continent, the SHT signal is weak and slightly positive. Therefore, for the mechanism discussion, we will show both coastal and broader domains.

4 **Mechanism**

The driving force behind how and why frequency metrics change, regionally, in a warming world (i.e., more or less ARs) can be tied to their response to jets and the zonal wind (Shields and Kiehl, 2016a and 2016b; Payne and Magnosdottir 2015). As seen from Equations (1) and

(2), however, heat transport is driven by the meridional wind. Therefore, the response of the meridional wind to climate change needs to be considered. Climate change meridional wind (300 hPa and 850 hPa) climatologies for WNAM and UK domains (180W-90W, 50W-30E, respectively) and coastlines (130W-110W, 30W-0E) are illustrated via Hovmöller diagram in Figures 4 (WNAM) and 5, (UK) left and center-left panels. For points of reference and a holistic view of the components of heat transport, historical and RCP8.5 climatologies are plotted with variance values in Figures S5-8 along with temperature and specific humidity changes (SF9-10). Monthly climatologies start in July and progress through June to emphasize the cool season months and peak AR activity (Neiman et al., 2008; Lavers et al. 2010; Ramos et al., 2015). Statistical significance, shown with stippling at the 95% level, shows broad areas of significant change for the meridional wind at both 300 and 850 hPa for all domains. Transport terms for sensible heat (center-right panels) and latent heat (right panels) are also plotted in the same style to compare spatial patterns with significance testing relaxed to the 90% level. For simplicity we only show transport terms from landfalling UK ARs, which have a signature similar to Iberian ARs. The coastal domain patterns in Figures 4 and 5, primarily peak between 30^{o} and 60^{o}N for both SHT and LHT consistent with the location of peak ARs frequency. Climate change in meridional heat transport is clearly well correlated to the meridional wind although SHT is far stronger than LHT. Key winter months and the seasonal progression from boreal winter into spring from lower to mid-latitudes align very well with upper-level wind. (Note that, as in Figures 1-3, the absolute values of LHT are approximately an order of magnitude less than

SHT). The emphasis on late summer and early fall for WNAM LHT is likely, in part, due to background moisture availability in a warmer world, under the Clausius-Clapeyron relationship, compared to the historical period. For the broader "life cycle" domain, reductions in WNAM SHT reflect elements of both upper and lower meridional wind response, as do LHT, but with less significance. The broad pattern of reductions in LHT is consistent with weaker winds in the lower-mid-latitudes and stronger winds in the upper-mid-latitudes. For the larger UK domain, the pattern approximates the coastal pattern with the highest significance in the LHT term and peak changes occurring in the shoulder seasons, a finding consistent with projected changes in AR frequency (Shields et al., 2016, Warner et al, 2015).

5 Discussion and Summary

We diagnose meridional heat transport by atmospheric rivers for three regions commonly affected by landfalling ARs, using both MERRA-2 and high-resolution CESM1.3 model data. We explicitly compute both meridional SHT and LHT for landfalling ARs impacting western North America, the UK, and the Iberian Peninsula using MERRA-2, ARTMIP Tier 1 catalogues, and CESM1.3 data. We show that there is general agreement in both transport quantities and latitudinal distribution for these terms across ARTMIP members for the MERRA-2 data, as well as across MERRA-2 reanalysis data and CESM1.3 historical model output. Under global warming, using the SK2016 algorithm and high-resolution CESM1.3 climate change model

output, we show that latent heat transport increases across all regions in the mid-latitudes although there is a different latitudinal signature for AR-days compared to the all days across the full record. For sensible heat transport, western North America (Europe) is projected to experience less (more) heat transport by ARs. The mechanism driving the changes in meridional heat transport by ARs can be primarily tied to upper-level meridional winds, although regional differences exist. Coastal domains provide a focused view of heat transport by landfalling ARs, while the broader domains inform the larger-scale response. Mechanistic differences between regional ARs in the context of heat transport are evident, in particular for LHT, and illustrate the importance of evaluating ARs from a regional perspective where the climate change response depends on the flavor of AR.

Acknowledgments

There are many institutions, programs, and people to thank for the enormous undertaking of high-resolution simulations. They include: Regional and Global Model Analysis (RGMA) component of EESMP of the U.S. DOE's BER via National Science Foundation (NSF) IA 1947282; National Center for Atmospheric Research (NCAR), sponsored by NSF under

Cooperative Agreement No. 1852977; CESM is supported primarily by NSF; Climate Simulation Laboratory within NCAR's Computational and Information Systems Laboratory (doi:10.5065/D6RX99HX), sponsored by NSF and other agencies; Innovative and Novel Computational Impact on Theory and Experiment (INCITE) program and Argonne Leadership Computing Facility, contract DE-AC02-06CH11357; Blue Waters sustained-petascale computing project, supported by NSF (awards OCI-0725070 and ACI-1238993) and the state of Illinois (a joint effort of the University of Illinois at Urbana-Champaign and its National Center for Supercomputing Applications, "High Resolution Earth System Modeling Using Blue Waters Capabilities" PRAC NSF award number ACI-1516624). ARTMIP includes international researchers from universities, laboratories, and agencies. Co-chairs and committee members are Jonathan Rutz, Christine Shields, Ruby Leung, Marty Ralph, Ashley Payne, Travis O'Brien, and Michael Wehner. Details on catalogues developers can be found on the ARTMIP website. ARTMIP has received support from the US DOE (BER) as part of the RGCM, and the Center for Western Weather and Water Extremes (CW3E) at Scripps Institute for Oceanography at the University of California, San Diego. Finally, we thank Brian Medeiros and James Benedict for sharing their MERRA-2 daily data, and Jeff Kiehl for insight on heat transport.

Data Availability

ARTMIP data is available from the Climate Data Gateway, DOI:10.5065/D6R78D1M (ARTMIP Tier 1 catalogues), DOI: 10.5065/D62R3QFS (MERRA-2 source data). Data from all analysis

presented here is available through the Climate Data Gateway. High-resolution CESM1.3 simulations are available on NCAR's long term archiving facility.

References

Armour, K.C., N. Siler, A. Donohoe, and G.H. Roe (2019): Meridional Atmospheric Heat Transport Constrained by Energetics and Mediated by Large-Scale Diffusion. *J. Climate*, **32**, 3655–3680, https://doi.org/10.1175/JCLI-D-18-0563.1.

Barry, L., Craig, G. C., & Thuburn, J. (2002). Poleward heat transport by the atmospheric heat engine. Nature, 415(6873), 774–777. https://doi.org/10.1038/415774a

Bonne, J., H. C. Steen-Larsen, C. Risi, M. Werner, H. Sodemann, J. Lacour, X. Fettweis, G. Cesana, M. Delmotte, O. Cattani, P. Vallelonga, H. A. Kjær, C. Clerbaux, Á. E. Sveinbjörnsdóttir, and V. Masson-Delmotte (2015), The summer 2012 Greenland heat wave: In situ and remote sensing observations of water vapor isotopic composition during an atmospheric river event. J. Geophys. Res. Atmos., 120, 2970–2989. doi: 10.1002/2014JD022602.

Brands, S., Gutiérrez, J. M., & San-Martín, D. (2016), Twentieth-century atmospheric river activity along the west coasts of Europe and North America: algorithm formulation, reanalysis

uncertainty and links to atmospheric circulation patterns. Climate Dynamics, 48(9–10), 2771–2795. https://doi.org/10.1007/s00382-016-3095-6.

Chang, E. K. M., Y. Guo, and X. Xia (2012), CMIP5 multimodel ensemble projection of storm track change under global warming, J. Geophys. Res., 117, D23118, doi:10.1029/2012JD018578.

Colman, R.A., McAvaney, B.J., Fraser, J.R. et al. (1994) Climate Dynamics, Annual mean meridional energy transport modeled by a general circulation model for present and 2 x CO2 equilibrium climates, 10, pp221 -229, https://doi.org/10.1007/BF00208989.

Dacre, H. F., P. A. Clark, O. Martinez-Alvarado, M. A. Stringer, and D. A. Lavers (2015), How do atmospheric rivers form?, Bull. Am. Meteorol. Soc., 96(8), 1243–1255.

Dee, D. P., et al., (2011), The ERA-Interim reanalysis: configuration and performance of the data assimilation system, Q. J. R. Meteorol. Soc., 137(656), 553-597.

Dettinger, M.D. (2011), Climate change, atmospheric rivers, and floods in California—A multimodel analysis of storm frequency and magnitude changes, J. Am. Water Resour. Assoc., 47(3), 514–523.

Dettinger, M.D., F.M. Ralph, T. Das, P.J. Neiman, and D. Cayan (2011), Atmospheric rivers, floods, and the water resources of California, Water, 3, 455-478

Dettinger, M.D. (2013), Atmospheric Rivers as Drought Busters on the U.S. West Coast, Journal of Hydrometeorology, 14:6, 1721-1732.

Espinoza, V., Waliser, D. E., Guan, B., Lavers, D. A., & Ralph, F. M. (2018), Global analysis of climate change projection effects on atmospheric rivers. *Geophysical Research Letters*, 45, 4299–4308. https://doi.org/10.1029/2017GL076968.

Gao, Y., J. Lu, L. R. Leung, Q. Yang, S. Hagos, and Y. Qian (2015), Dynamical and thermodynamical modulations on future changes of landfalling atmospheric rivers over western North America, Geophys. Res. Lett., 42, 7179–7186, doi:10.1002/2015GL065435.

Gao, Y., J. Lu, and L. R. Leung (2016), Uncertainties in projecting future changes in atmospheric rivers and their impacts on heavy precipitation over Europe, J. Clim., doi:10.1175/JCLI-D-16-0088.1.

Gershunov, A, T. Shulgina, F.M. Ralph, D.A. Laver, and J.J Rutz, (2017), Assessing the climate-scale variability of atmospheric rivers affecting western North America, Geophys. Res. Lett., 44, 7900–7908.

Goldenson, N., L.R. Leung, C.M. Bitz, and E. Blanchard-Wrigglesworth (2018), Influence of Atmospheric Rivers on Mountain Snowpack in the Western United States. *J. Climate,* **31**, 9921–9940, https://doi.org/10.1175/JCLI-D-18-0268.1.

Gonzales, K. R., Swain, D. L., Nardi, K. M., Barnes, E. A., & Diffenbaugh, N. S. (2019), Recent warming of landfalling atmospheric rivers along the west coast of the United States. *Journal of Geophysical Research: Atmospheres*, 124, 6810– 6826. https://doi.org/10.1029/2018JD029860.

Gorodetskaya, I. V., Tsukernik, M., Claes, K., Ralph, M. F., Neff, W. D. and Van Lipzig, N. 15 P. M. (2104), The role of atmospheric rivers in anomalous snow accumulation in East Antarctica, Geophysical Research Letters, 41(17), 6199–6206, doi:10.1002/2014gl060881, 2014.

Guan, B., D.E. Waliser, N.P. Molotch, E.J. Fetzer, and P.J. Neiman, (2012), Does the Madden–Julian Oscillation Influence Wintertime Atmospheric Rivers and Snowpack in the Sierra Nevada?. Mon. Wea. Rev., 140, 325–342, https://doi.org/10.1175/MWR-D-11-00087.1

Guan, B., and D. E. Waliser (2015), Detection of atmospheric rivers: Evaluation and application of an algorithm for global studies, *J. Geophys. Res. Atmos.*, 120, 12514–12535, doi: 10.1002/2015JD024257.

Hagos, S.M., L.R. Leung, J.-H. Yoon, J. Lu, and Y. Gao (2016), A projection of changes in landfalling atmospheric river frequency and extreme precipitation over western North America from the large ensemble CESM simulations. *Geophys. Res. Lett.*, 43, 1357–1363, doi: 10.1002/2015GL067392.

Hagos, S.M., L. Ruby Leung, Qing Yang, Chun Zhao, and Jian Lu (2015), Resolution and Dynamical Core Dependence of Atmospheric River Frequency in Global Model Simulations, Journal of Climate 2015 28:7, 2764-2776.

Hunke, E.C., and W.H. Lipscomb (2008), CICE: The Los Alamos sea ice model user's manual, version 4. Los Alamos National Laboratory Tech. Rep. LA-CC-06-012, 76pp.

Kiehl, J. T., Shields, C. A., Snyder, M. A., Zachos, J. C., & Rothstein, M. (2018). Greenhouse- and orbital-forced climate extremes during the early Eocene. Philosophical Transactions of the

Royal Society A: Mathematical, Physical and Engineering Sciences, 376(2130), 20170085. https://doi.org/10.1098/rsta.2017.0085.

Lawrence, D. M., et al. (2011), Parameterization improvements and functional and structural advances in version 4 of the Community Land Model. J. Adv. Model. Earth Syst., 3, M03001, doi:10.1029/2011MS000045.

Lavers, D. A., G. Villarini, R. P. Allan, E. F. Wood, and A. J. Wade (2012), The detection of atmospheric rivers in atmospheric reanalyses and their links to British winter floods and the large-scale climatic circulation, J. Geophys. Res., 117, D20106, doi:10.1029/2012JD018027.

Lavers, D. A., and G. Villarini (2013), The nexus between atmospheric rivers and extreme precipitation across Europe, Geophys. Res. Lett., 40, 3259–3264, doi:10.1002/grl.50636.

Lavers, D. A., R. P. Allan, G. Villarini, B. Lloyd-Hughes, D. J. Brayshaw, and A. J. Wade (2013), Future changes in atmospheric rivers and their implications for winter flooding in Britain, Environ. Res. Lett., 8, 034010, doi:10.1088/1748-9326/8/3/034010.

Lavers, D. A., & Villarini, G. (2015), The contribution of atmospheric rivers to precipitation in Europe and the United States. Journal of Hydrology, 522, 382–390. https://doi.org/10.1016/j.jhydrol.2014.12.010.

Lavers, D.A., F.M. Ralkph, D.E. Waliser, A. Gershunov, and M.D. Dettinger (2015), Climate change intensification of horizontal water vapor transport in CMIP5, Geophys. Res. Lett., 42, doi:10.1002/2015GL064672.

Lora, J. M., Mitchell, J. L., Risi, C. and Tripati, A. E. (2017), North Pacific atmospheric rivers and 15 their influence on western North America at the Last Glacial Maximum, Geophysical Research Letters, 44(2), 1051–1059, doi:10.1002/2016gl071541.

Mundhenk, B.D., E.A. Barnes, and E.D. Maloney (2016), All-Season Climatology and Variability of Atmospheric River Frequencies over the North Pacific. *J. Climate*, **29**,4885–4903, https://doi.org/10.1175/JCLI-D-15-0655.1.

Muszynski, G., Kashinath, K., Kurlin, V., Wehner, M., and Prabhat, (2018), Topological Data Analysis and Machine Learning for Recognizing Atmospheric River Patterns in Large Climate Datasets, Geosci. Model Development, https://doi.org/10.5194/gmd-2018-53.

Neale, R. B., and Coauthors, 2010: Description of the NCAR Community Atmosphere Model (CAM5.0). NCAR Tech. Rep. NCAR/TN-486+STR, 268 pp.

Neiman, P. J., L. J. Schick, F. M. Ralph, M. Hughes, and G. A. Wick (2011), Flooding in Western Washington: The Connection to Atmospheric Rivers, J. Hydrometeorol., 12(6), 1337-1358.

Neiman, P.J., F.M. Ralph, G.A. Wick, J.D. Lundquist, and M.D. Dettinger (2008), Meteorological characteristics and overland precipitation impacts of atmospheric rivers affecting the West Coast of North America based on eight years of SSM/I satellite observations, J. Hydrometeo., 9, 22-47.

Newman, M., G.N. Kiladis, K.M. Weickmann, F.M. Ralph, and P.D. Sardeshmukh (2012), Relative contributions of synoptic and low-frequency eddies to time-mean atmospheric moisture transport, including the role of atmospheric rivers, J. Climate, 25, 7341-7361.

O'Gorman, P. A. (2010), Understanding the varied response of the extratropical storm tracks to climate change. Proceedings of the National Academy of Sciences, 107(45), 19176–19180. https://doi.org/10.1073/pnas.1011547107.

Park, S., C. S. Bretherton, and P. J. Rasch, (2014), Integrating cloud processes in the Community Atmosphere Model, Version 5. *J. Clim.*, **27**, 6821-6856.

Meehl, G. A., Yang, D., Arblaster, J. M., Bates, S. C., Rosenbloom, N., Neale, R., et al (2019). Effects of model resolution, physics, and coupling on Southern Hemisphere storm tracks in CESM1.3. Geophysical Research Letters, 46. https://doi.org/10.1029/2019GL084057.

Mizuta, R. (2012), Intensification of extratropical cyclones associated with the polar jet change in the CMIP5 global warming projections, Geophys. Res. Lett., 39, L19707, doi:10.1029/2012GL053032.

Pan, Y., Li, L., Jiang, X., Li, G., Zhang, W., Wang, X., & Ingersoll, A. P. (2017), Earth's changing global atmospheric energy cycle in response to climate change. Nature Communications, 8, 14367, https://doi.org/10.1038/ncomms14367.

Payne, A.E. and G. Magnusdottir, (2014), Dynamics of Landfalling Atmospheric Rivers over the North Pacific in 30 Years of MERRA Reanalysis. *J. Climate*, **27**, 7133–7150,https://doi.org/10.1175/JCLI-D-14-00034.1.

Payne, A. E., and G. Magnusdottir (2015), An evaluation of atmospheric rivers over the North Pacific in CMIP5 and their response to warming under RCP 8.5, *J. Geophys. Res. Atmos.*, 120, 11,173–11,190, doi:10.1002/2015JD023586.

Ralph, F. M., P. J. Neiman, and G. A. Wick (2004), Satellite and CALJET aircraft observations of atmospheric rivers over the eastern North-Pacific Ocean during the El Niño winter of 1997/98. Mon. Wea. Rev., 132, 1721-1745.

Ralph, F.M., P.J. Neiman, R. Rotunno, (2005), Dropsonde Observations in Low-Level Jets over the Northeastern Pacific Ocean from CALJET-1998 and PACJET-2001: Mean Vertical-Profile and Atmospheric-River Characteristics, Mon. Wea. Rev., doi:10.1175/MWR2896.1.

Ralph, F. M., P. J. Neiman, G. A. Wick, S. I. Gutman, M. D. Dettinger, D. R. Cayan, and A. B. White, (2006), Flooding on California's Russian River: Role of atmospheric rivers, GRL, doi:10.1029/2006GL026689.

Ralph, F.M., P.J. Neiman, G. N. Kiladis, K. Weickmann, D.W. Reynolds, (2011), A Multiscale Observational Case Study of a Pacific Atmospheric River Exhibiting Tropical Extratropical Connections and a Mesoscale Frontal Wave, Mon. Wea. Rev., doi: 10.1175/2010MWR3596.1.

Ralph, F. M., T. Coleman, P.J. Neiman, J. Zamora, M.D. Dettinger, (2013), Observed Impacts of Duration and Seasonality of Atmospheric-River Landfalls on Soil Moisture and Runoff in Coastal Northern California, J. of Hydro. Meteorology, doi: 10.1175/JHM-D-12-076.1.

Ralph, F.M., S.F. Iacobellis, P.J. Neiman, J.M. Cordeira, J.R. Spackman, D.E. Waliser, G.A. Wick, A.B. White, and C. Fairall, (2017a), Dropsonde Observations of Total Integrated Water Vapor Transport within North Pacific Atmospheric Rivers. J. Hydrometeor., 18, 2577–2596, https://doi.org/10.1175/JHM-D-17-0036.1.

Ralph, F.M., M. Dettinger, D. Lavers, I.V. Gorodetskaya, A. Martin, M. Viale, A.B. White, N. Oakley, J. Rutz, J.R. Spackman, H. Wernli, and J. Cordeira, (2017b), Atmospheric Rivers

Emerge as a Global Science and Applications Focus. Bull. Amer. Meteor. Soc., 98, 1969–1973, https://doi.org/10.1175/BAMS-D-16-0262.1.

Ramos, A. M., Trigo, R. M., Liberato, M. L. R., & Tomé, R. (2015), Daily Precipitation Extreme Events in the Iberian Peninsula and Its Association with Atmospheric Rivers*. Journal of Hydrometeorology, 16(2), 579–597. https://doi.org/10.1175/jhm-d-14-0103.1.

Ramos A.M., R. Nieto, R. Tomé, L. Gimeno, R.M. Trigo, M.L.R. Liberato and D.A. Lavers (2016), Atmospheric rivers moisture sources from a Lagrangian perspective. Earth Syst. Dynam. 7: 371-384, https://doi.org/10.5194/esd-7-371-2016, 2016.

Rutz, J.J., W.J. Steenburgh, and F.M. Ralph, (2014), Climatological Characteristics of Atmospheric Rivers and Their Inland Penetration over the Western United States. *Mon. Wea. Rev.*, **142**, 905–921, https://doi.org/10.1175/MWR-D-13-00168.1.

Sellars, S.L., X. Gao, and S. Sorooshian, (2015), An Object-Oriented Approach to Investigate Impacts of Climate Oscillations on Precipitation: A Western United States Case Study. *J. Hydrometeor.,* **16**, 830–842, https://doi.org/10.1175/JHM-D-14-0101.1.

Shields, C. A., and J. T. Kiehl (2016a), Simulating the Pineapple Express in the half degree

Community Climate System Model, CCSM4, Geophys. Res. Lett., 43, doi:10.1002/2016GL069476.

Shields, C. A., and J. T. Kiehl (2016b), Atmospheric river landfall-latitude changes in future climate simulations, Geophys. Res. Lett., 43, 8775–8782, doi:10.1002/2016GL070470.

Shields, C.A., J.T. Kiehl, G.A. Meehl (2016c), Future Changes in Regional Precipitation Simulated by a Half-Degree Coupled Climate Model: Sensitivity to Horizontal Resolution, JAMES, doi: 10.1002/2015MS000584.

Siler, N., G.H. Roe, and K.C. Armour (2018), Insights into the Zonal-Mean Response of the Hydrologic Cycle to Global Warming from a Diffusive Energy Balance Model. *J. Climate*, **31**, 7481–7493, https://doi.org/10.1175/JCLI-D-18-0081.1.

Sousa, P.M., A.M. Ramos, C.C. Raible, M. Messmer, R. Tomé, J.G. Pinto, and R.M. Trigo, 2019: North Atlantic Integrated Water Vapor Transport – from 850-2100 CE: Impacts on Western European Rainfall. J. Climate, 0, https://doi.org/10.1175/JCLI-D-19-0348.1.

Smith, R. D., et al. (2010), The Parallel Ocean Program (POP) reference manual, Tech. Rep. LAUR-10-01853, Los Alamos Natl. Lab., Los Alamos. [Available

http://www.cesm.ucar.edu/models/cesm1.0/pop2/doc/sci/POPRefManual.pdf.]

Tamarin-Brodsky, T., & Kaspi, Y. (2017), Enhanced poleward propagation of storms under climate change. Nature Geoscience, 10(12), 908–913. https://doi.org/10.1038/s41561-017-0001-8.

Taylor, M. A., and A. Fournier (2010), A compatible and conservative spectral element method on unstructured grids. *J. Comput. Phys.*, **229**, 5879–5895, https://doi.org/10.1016/j.jcp.2010.04.008.

Vahedifard, F., AghaKouchak, A., Ragno, E., Shahrokhabadi, S., & Mallakpour, I. (2017), Lessons from the Oroville dam. Science, 355(6330), 1139.2-1140. https://doi.org/10.1126/science.aan0171.

Warner, M.D., C.F. Mass, E.P. Salathe, (2015), Changes in Winter Atmospheric Rivers along the North American West Coast in CMIP5 Climate Models, J. Hydro. Meteorology, doi:10.1175/JHM-D-14-0080.1.

Wu, Y., Ting, M., Seager, R., Huang, H.-P., & Cane, M. A. (2010), Changes in storm tracks and energy transports in a warmer climate simulated by the GFDL CM2.1 model. Climate Dynamics, 37(1–2), 53–72. https://doi.org/10.1007/s00382-010-0776-4.

Zhu, Y., and R. E. Newell (1998), A proposed algorithm for moisture fluxes from atmospheric rivers, Mon. Weather Rev., 126(3), 725–735, doi:10.1175/1520-0493(1998)126<0725:APAFMF>2.0.CO;2.

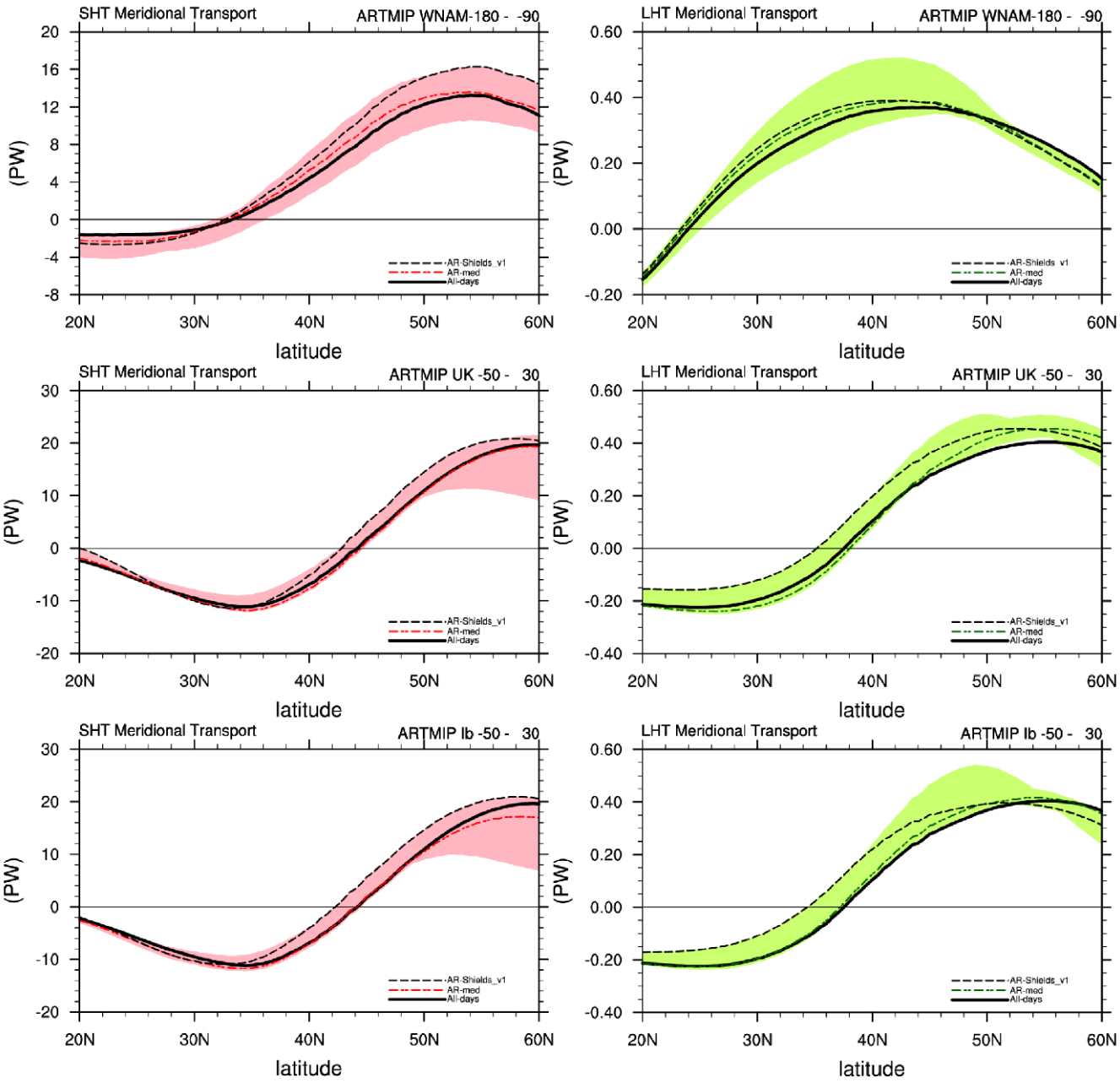

Figure 1. ARTMIP spread for MERRA-2 (1980-2016) heat transport via atmospheric river (AR) for sensible heat (left panels, red) and latent heat (right panels, green). ARTMIP median values

are dashed with the maximum and minimum highlighted with shading. Black dashed lines indicating where the Shields and Kiehl algorithm lies relative to the ARTMIP spread. Dark solid lines indicate full heat transport for All-days. WNAM (Western North America, top panels), UK (United Kingdom, middle panels), and Ib (Iberian Peninsula, bottom panels) are plotted (longitude range included in mean is given in parenthesis). Transport is computed as an annual mean and the units are in PW.

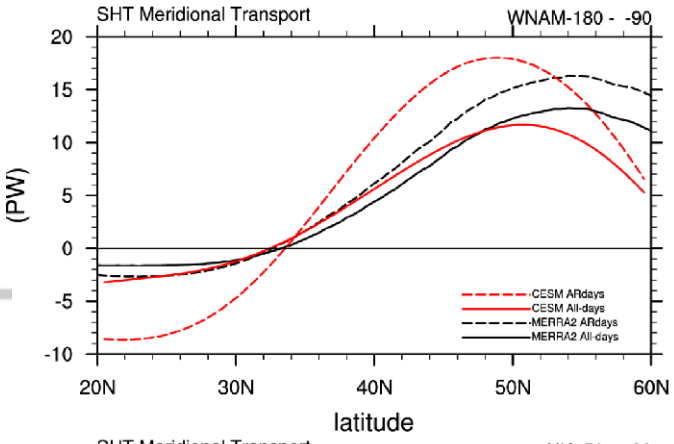

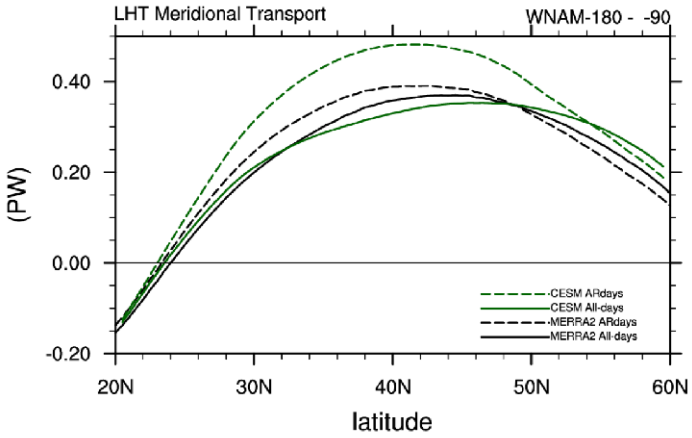

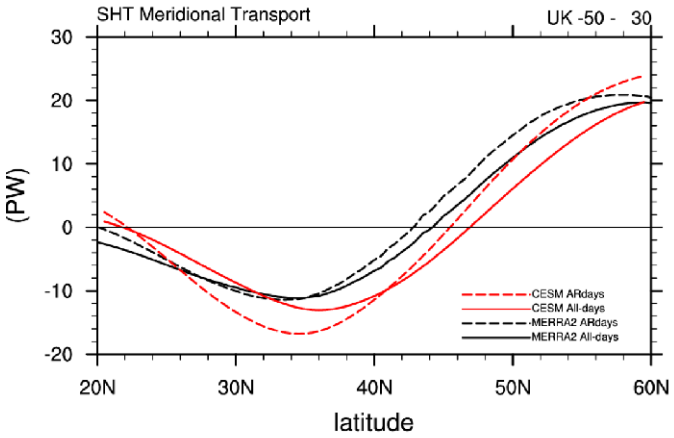

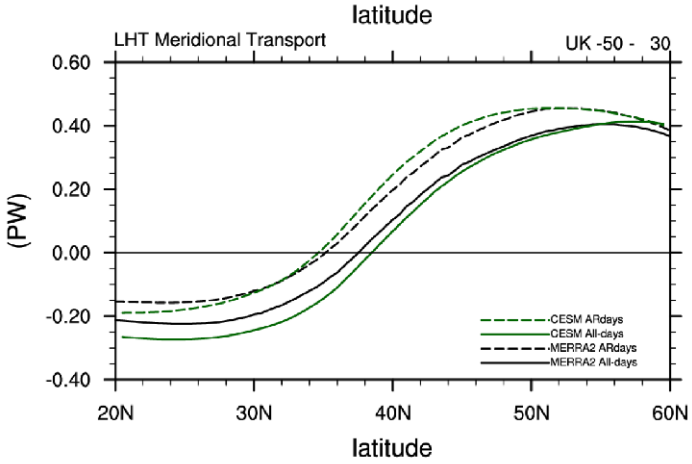

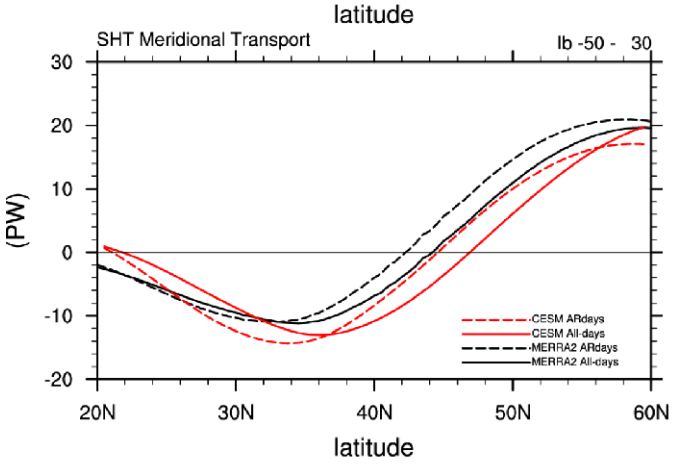

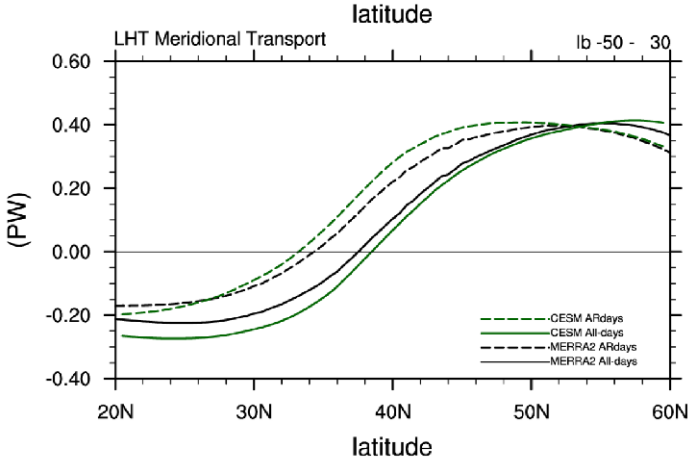

Figure 2. Similar to Figure 1 except MERRA-2 Shields-Kiehl AR catalogue (SK2016; black dashed line, years 1980-2016)) is compared to CESM1.3 historical simulations (red lines for sensible heat and green lines for latent heat, years 1991-2005). AR-days (dashed) are compared to All-days (solid).

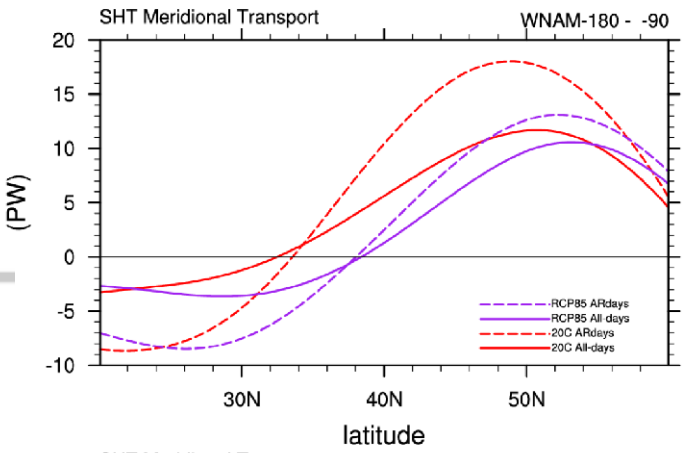

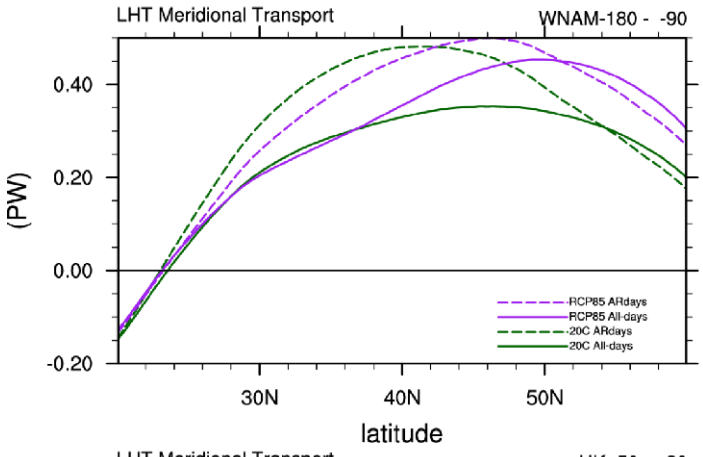

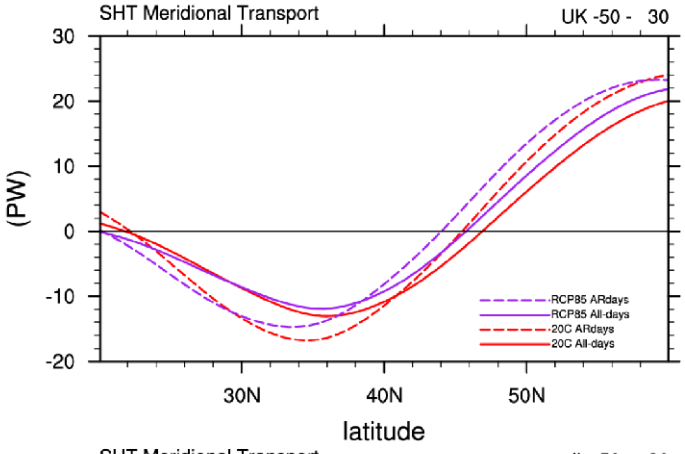

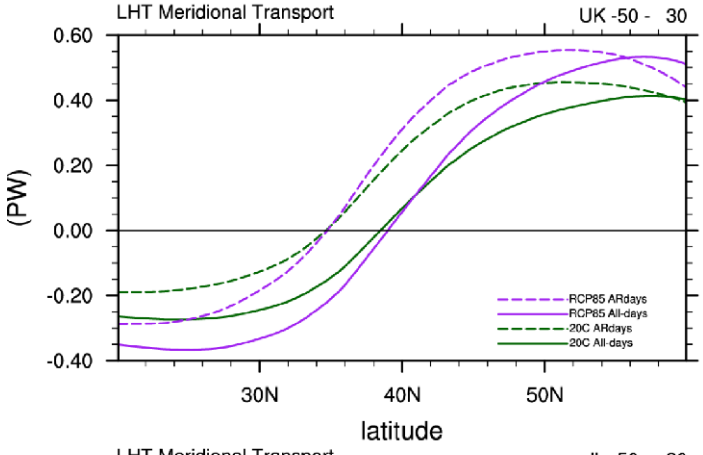

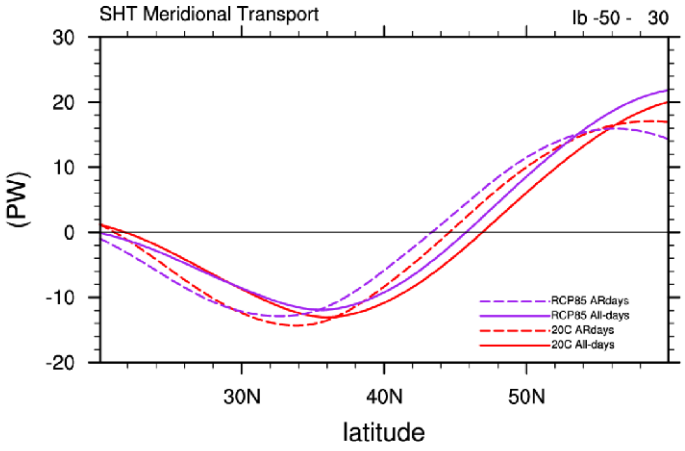

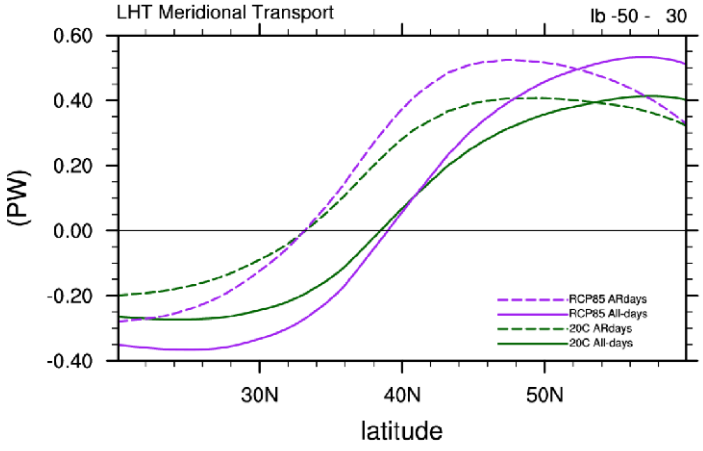

Figure 3. Similar to Figure 2 CESM1.3 historical simulations (red lines for sensible heat and green lines for latent heat, years 1991-2005) are compared to RCP8.5 simulations (purple lines, years 2070-2099). AR-days (dashed) are compared to All-days (solid).

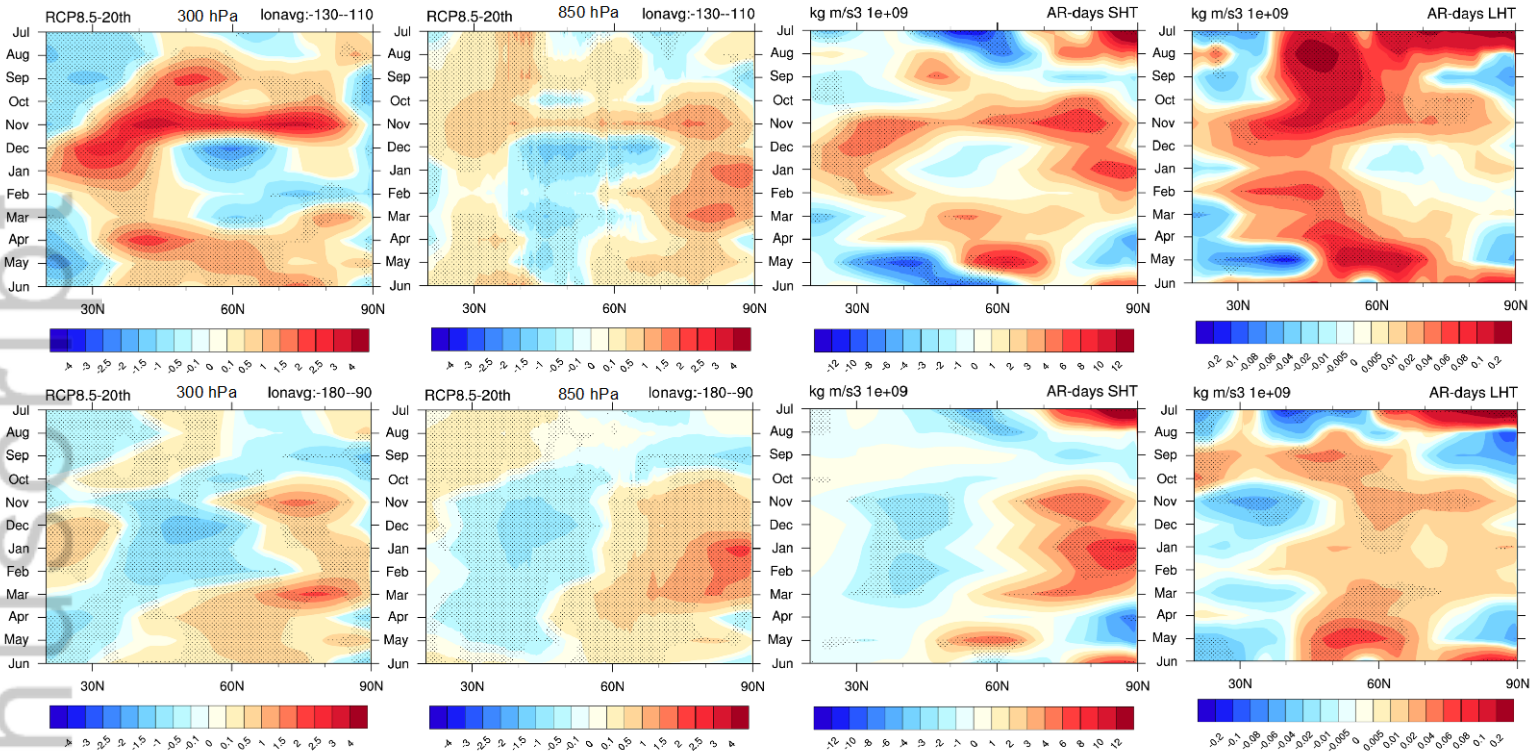

Figure 4. Western North American climate change (RCP8.5 – historical) mean annual cycle for 300hPa meridional wind (left panels), 850mb meridional wind (left-center panels), sensible heat term (right-center panels), and latent heat term (right panels). Energy terms are computed using AR-days for events making landfall over coastal regions where ARs make landfall (upper panels, averaged from 110W-130W), and the broad Pacific Ocean region upwind to landfalling ARs (lower panels, averaged from 180W – 90W). Units for wind and energy terms are ms^{-1} and kgm^{-3} x 10^{9}, respectively. Meridional wind differences significant at the 95% level are stippled whereas the energy terms are stippled at 90%. Meridional wind data is computed from monthly mean data, years 2070-299 (RCP8.5) and 1960-2005 (Historical).

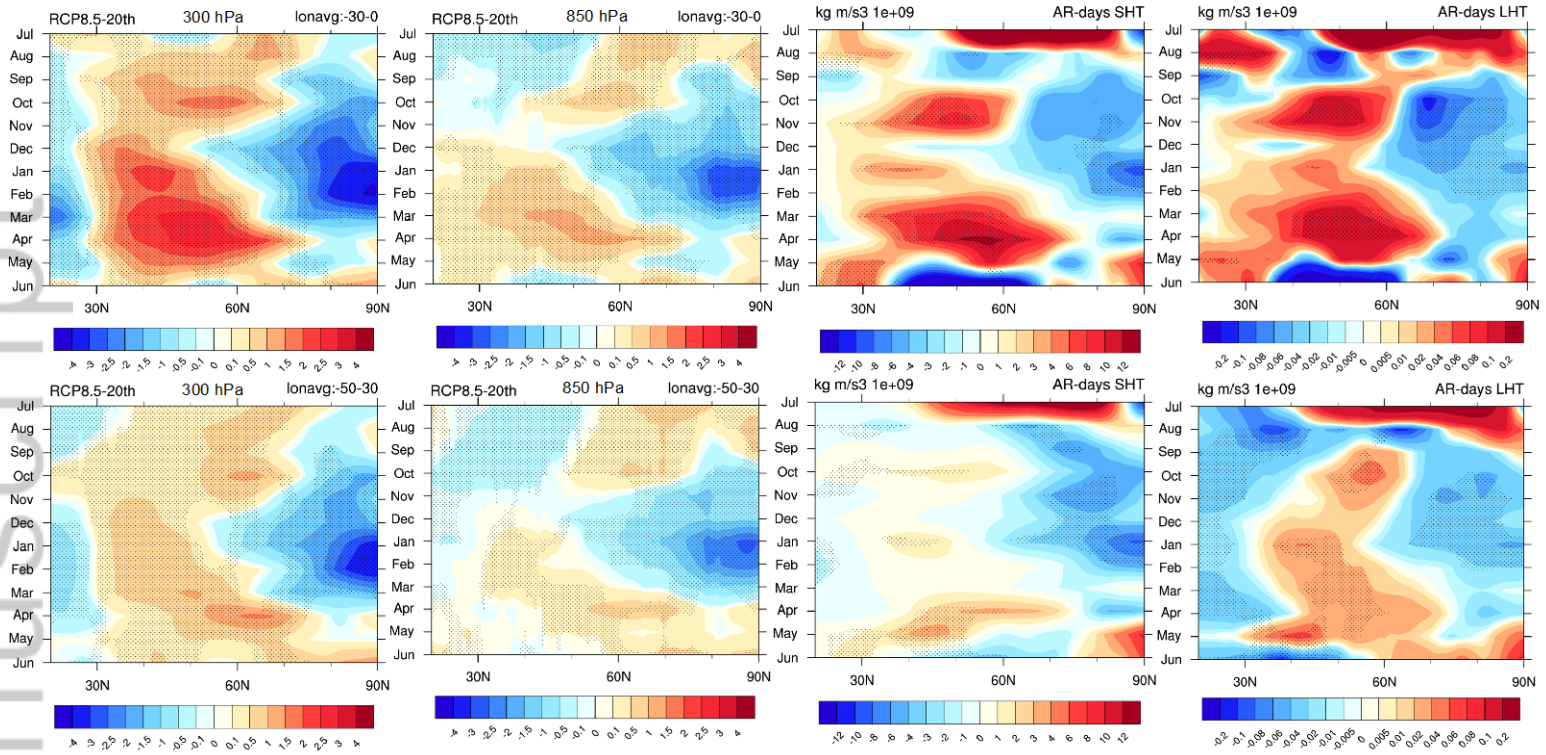

Figure 5. Same as Figure 4, except for European coastlines (averaged from 30W-0E) and the upwind Atlantic O cean region (50W-30E).